Associations between zircon and Fe–Ti oxides in Hiltaba event magmatic rocks, South Australia: atomic- or pluton-scale processes?

M. R. M. Ferguson[a]*, K. Ehrig[b], S. Meffre[a], and A. R. Cherry[a]

[a]ARC Centre of Excellence in Ore Deposits (CODES), School of Natural Sciences, University of Tasmania, Hobart, Tas 7001, Australia; [b]BHP Olympic Dam, 55 Grenfell Street, Adelaide, SA 5000, Australia

* Corresponding author. M. R. M Ferguson: matt.ferguson@utas.edu.au

Ferguson https://orcid.org/0000-0002-6137-1580
Ehrig https://orcid.org/0000-0002-5381-9445
Meffre https://orcid.org/0000-0003-2741-6076
Cherry https://orcid.org/0000-0001-5993-6311

SUPPLEMENTARY PAPERS

Australian Journal of Earth Sciences (2020) 67, doi:10.1080/08120099.2019.1653990

Copies of Supplementary Papers may be obtained from the Geological Society of Australia's website (www.gsa.org.au), the Australian Journal of Earth Sciences website (www.ajes.com.au) or from the National Library of Australia's Pandora archive (https://pandora.nla.gov.au/tep/150555).

Supplementary papers

Appendix A.1 Methods

A.1.1 Zircon U–Pb and trace-element analysis and data reduction (University of Tasmania).
A.1.2 Zircon trace-element analysis and data reduction (Boise State University).
A.1.3 Apatite U–Pb analysis and data reduction (University of Tasmania).
A.1.4 Ti-in-zircon thermometry.

Appendix A.2. Additional zircon trace element data; analytical areas; cathodoluminescence imagery.

Appendix B.1 In situ growth of zircon

Appendix B.2 Xenocrystic or autocrystic zircon?

Tables (excel file)

Table S1. Sample locations.
Table S2A. Zircon LA-ICPMS metadata.
Table S2B. Apatite LA-ICPMS metadata.
Table S3A. Zircon geochronology.
Table S3B. Apatite geochronology.
Table S4. Zircon trace-element data.
Table S5. Zr-bearing phase data.
Table S6. Titanite geochronology.

A.1 Methods

A.1.1 Zircon U–Pb and trace element analysis and data reduction (University of Tasmania)

Zircon U–Pb and trace element analyses were performed on an Agilent 7900 quadropole ICPMS, coupled to a Coherent COMPex Pro 193 nm ArF Excimer laser system equipped with a Laurin Technic (Resolution S155) constant geometry ablation cell at the School of Earth Sciences, University of Tasmania. Each analysis was pre-ablated with 5 laser pulses to remove any surface contamination. Blank gas was analysed for 20 s followed by 20 s of zircon ablation with operating conditions of 5 Hz and ~2 J/cm^2 using a spot size of 29 μm. Helium carrier gas flowing at 0.35 l/min carried particles ablated by the laser out of the sample chamber to be mixed with Ar gas before transfer to the plasma. Elements measured include ^{49}Ti, ^{89}Y, ^{91}Zr, ^{139}La, ^{140}Ce, ^{141}Pr, ^{146}Nd, ^{147}Sm, ^{153}Eu, ^{157}Gd, ^{159}Tb, ^{163}Dy, ^{165}Ho, ^{166}Er, ^{169}Tm, ^{172}Yb, ^{175}Lu, ^{178}Hf, ^{202}Hg, ^{204}Pb, ^{206}Pb, ^{207}Pb, ^{208}Pb, ^{232}Th, ^{235}U and ^{238}U. Each element was measured sequentially every 0.24 s with longer counting time on the Pb isotopes compared to the other elements. Lower age precision due to longer sweep times is acceptable and age data is used for comparative purposes only; much greater precision has been achieved in other studies of the GRV and HS (e.g. Cherry, Ehrig, et al., 2018; Jagodzinski, 2005; Jagodzinski et al., 2016; Jagodzinski et al., submitted). The down hole fractionation, instrument drift and mass bias correction factors for Pb/U and Pb/Th ratios on zircon analyses were calculated using two analyses of the primary standard (91500 of Wiedenbeck et al., 1995) and one analysis of each of the secondary standard zircons (TEMORA of Black et al., 2003; Plešovice of Sláma et al., 2008). Standards were analysed at the beginning and end of the sessions and every ~30 unknowns using the same spot size and conditions as used on the samples to provide an independent control to assess accuracy and precision. The correction factor for the ^{207}Pb/^{206}Pb ratio was calculated using the international glass standard NIST610 analysed throughout the sessions and corrected using the values recommended by Baker, Peate, Waight, and Meyzen (2004).

All data reduction calculations and error propagations were done within Microsoft Excel® via macros designed at the University of Tasmania, and using techniques summarised by Meffre et al. (2008) and Sack et al. (2011). Element abundances were calculated using Zr as the internal standard elements for zircon, assuming stoichiometric proportions and using the NIST 610 standard to correct for mass bias and drift. Interrogation of time-resolved signals allowed for identification of isotopic heterogeneity within the ablation volume. Time-resolved isotopic ratios for each analysis were scrutinised on U–Pb concordia diagrams to investigate the presence of common Pb and/or ancient Pb-loss and/or mixing of age zones; analyses (or parts of analyses) were excluded from the dataset where any of these trends was detected, utilising a similar approach to that of Petrus and Kamber (2012). Uncertainties were calculated using similar techniques to those outlined by Paton et al. (2010). Tera-Wasserburg diagrams and age calculations were made using Isoplot v4.15 (Ludwig, 2012).

The primary zircon standard 91500 yields a ^{207}Pb/^{206}Pb weighted mean age of 1067 ± 10 Ma (n = 78, MSWD = 0.76, P = 0.94), and a ^{206}Pb/^{238}U weighted mean age of 1063.4 ± 2.4 Ma (n = 78, MSWD = 0.29, P = 1), within uncertainty of published TIMS zircon ages of 1066.0 ± 0.6 Ma and 1063.5 ± 0.4 Ma (Horstwood *et al.,* 2016), respectively, indicating that the minimum level of uncertainty for our method is approximately 1%. The primary glass standard NIST610 yields a ^{207}Pb/^{206}Pb ratio of 0.90929 ± 0.00076 (n = 71, MSWD = 0.56, P = 0.999), within error of the recommended ^{207}Pb/^{206}Pb ratio of 0.90986 ±0.0001 (Baker et al., 2004). The secondary zircon standard Temora yields a ^{206}Pb/^{238}U weighted mean age of 415.0 ± 1.8 (n = 35, MSWD = 1.15, P = 0.26), within error of published TIMS zircon age of 416.8 ± 1.1 Ma (Black *et al.,* 2003). The secondary zircon standard Plesovice yields a ^{206}Pb/^{238}U weighted mean age of 338.9 ± 1.1 (n = 30, MSWD = 0.99, P = 0.48) within uncertainty of published TIMS zircon age of 337.13 ± 0.37 Ma (Sláma *et al.,* 2008).

A.1.2 Zircon trace element analysis and data reduction (Boise State University)

Zircon grains were separated from rocks using standard techniques, annealed at 900°C for 60 hours in a muffle furnace, and mounted in epoxy and polished until their centers were exposed. Cathodoluminescence (CL) images were obtained with a JEOL JSM-1300 scanning electron microscope and Gatan MiniCL. Zircon was analyzed by laser ablation inductively coupled plasma mass spectrometry (LA-ICPMS) using a ThermoElectron X-Series II quadrupole ICPMS and New Wave Research UP-213 Nd:YAG UV (213 nm) laser ablation system. In-house analytical protocols, standard materials, and data reduction software were used for acquisition and calibration of a suite of high field strength elements (HFSE) and rare earth elements (REE). Zircon was ablated with a laser spot of 25 μm wide using fluence and pulse rates of 5 J/cm^2 and 10 Hz, respectively, during a 45 second analysis (15 sec gas blank, 30 sec ablation) that excavated a pit ~25 μm deep. Ablated material was carried by a 1.2 L/min He gas stream to the nebuliser flow of the plasma. Dwell times were 5 ms for Si and Zr, 200 ms for ^{49}Ti and ^{207}Pb, 80 ms for ^{206}Pb, 40 ms for ^{202}Hg, ^{204}Pb, ^{208}Pb, ^{232}Th, and ^{238}U and 10 ms for all other HFSE and REE. Background count rates for each analyte were obtained prior to each spot analysis and subtracted from the raw count rate for each analyte. Ablations pits that appear to have intersected glass or mineral inclusions were identified based on Ti and P. For concentration calculations, background-subtracted count rates for each analyte were internally normalised to ^{29}Si and calibrated with respect to NIST SRM-610 and -612 glasses as the primary standards.

A.1.3 Apatite U–Pb analysis and data reduction (University of Tasmania)

Analyses of apatite for U–Pb geochronology were performed on an Agilent 7900 quadropole ICPMS, coupled to a Coherent COMPex Pro 193 nm ArF Excimer laser system equipped with a Laurin Technic (Resolution S155) constant geometry ablation cell at the School of Earth Sciences, University of Tasmania. All apatite analyses with associated reference materials were ablated with a 29 μm spot size at 5Hz and ~2 J/cm^2 laser fluence and were completed in a single session (measured isotopes: ^{31}P, ^{43}Ca, ^{56}Fe, ^{89}Y, ^{140}Ce, ^{202}Hg, ^{204}Pb, ^{206}Pb, ^{207}Pb, ^{208}Pb, ^{232}Th and ^{238}U). The 401 apatite (Thompson *et al.*, 2016) was used as a primary in-house geochronology reference material for calibration of Pb/U ratios and to correct for instrument drift (e.g. Huang *et al.*, 2016; Huang *et al.*, 2015). Calibration of the ^{207}Pb/^{206}Pb ratio was done using analyses of the NIST610 reference glass analysed at the same conditions as the unknowns. The Kovdor (Amelin & Zaitsev, 2002), McClure Mountain (Schoene & Bowring, 2006) and Otter Lake (Barfod, Krogstad, Frei, & Albarède, 2005) apatites were employed as secondary geochronology reference materials and were treated as unknowns (published and measured ages of the secondary reference materials are reported in Supplementary Data Table S2B).

A.1.4 Ti-in-zircon thermometry

Watson, Wark, and Thomas (2006) and Watson and Harrison (2005) define a zircon thermometer according to the dependence of Ti concentration in zircon on crystallisation temperature. Ferry and Watson (2007) have since further revised the thermometer calculation to allow for undersaturation in both rutile and quartz by incorporating a_{TiO_2} and a_{SiO_2}, following the equation:

$$T(\mathrm{K}) = \frac{-4{,}800 \pm 86}{\log \mathrm{Ti(ppm)} + \log a_{SiO_2} - \log a_{TiO_2} - (5.711 \pm 0.072)}$$

Correct application of this thermometer requires estimates of a_{TiO_2} and a_{SiO_2} at the time of zircon crystallisation. The presence of quartz in all units necessitates a relatively high a_{SiO_2}, so we held a_{SiO_2} constant at 1, which also maximises zircon crystallisation temperature estimates. Ilmenite and titanite in the lavas and granites indicates that a_{TiO_2} was not low (Hayden & Watson, 2007). We used a constant a_{TiO_2} of 0.7 for calculation of Ti-in-zircon temperatures.

Appendix A.2. Additional zircon trace element data; analytical areas; cathodoluminescence imagery

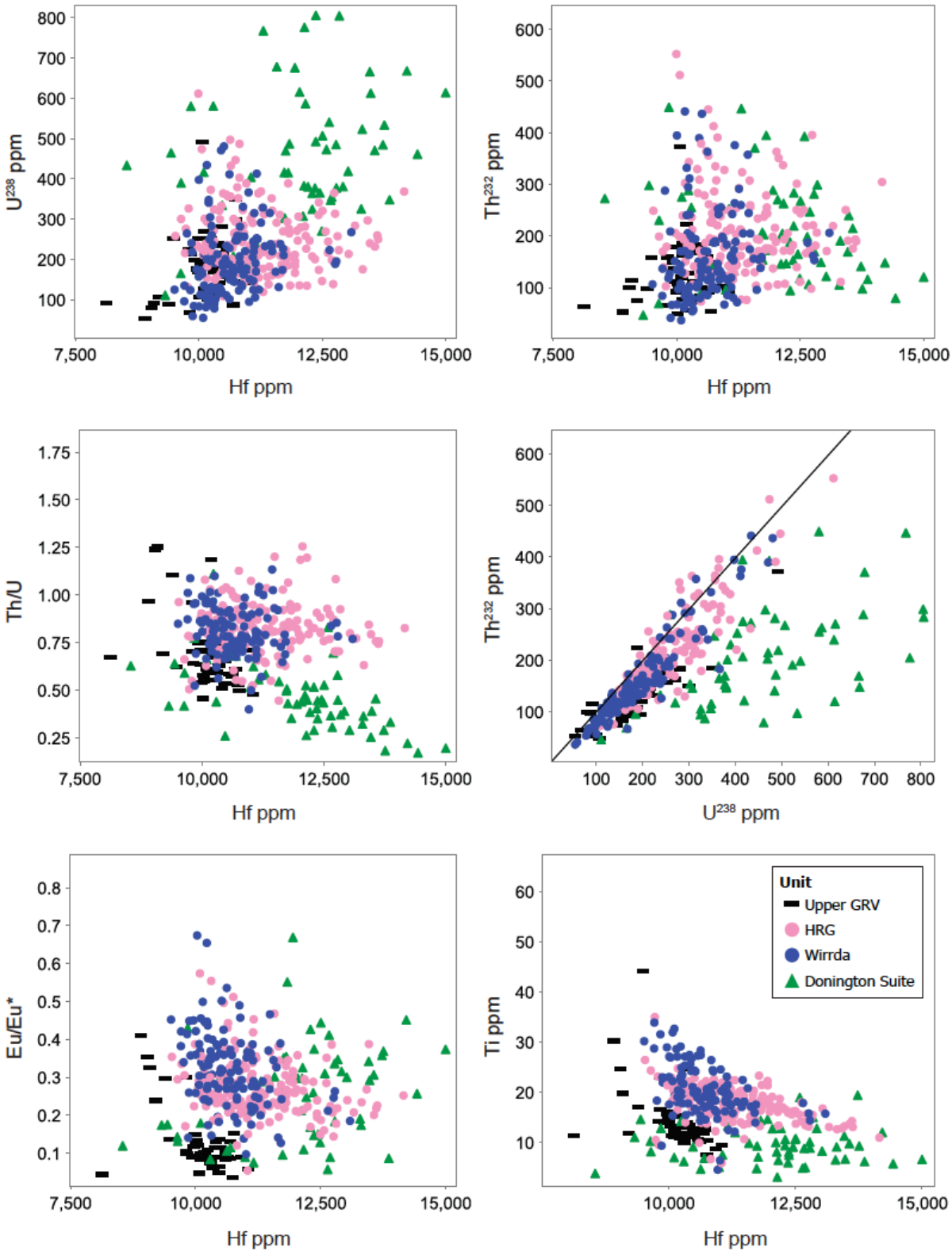

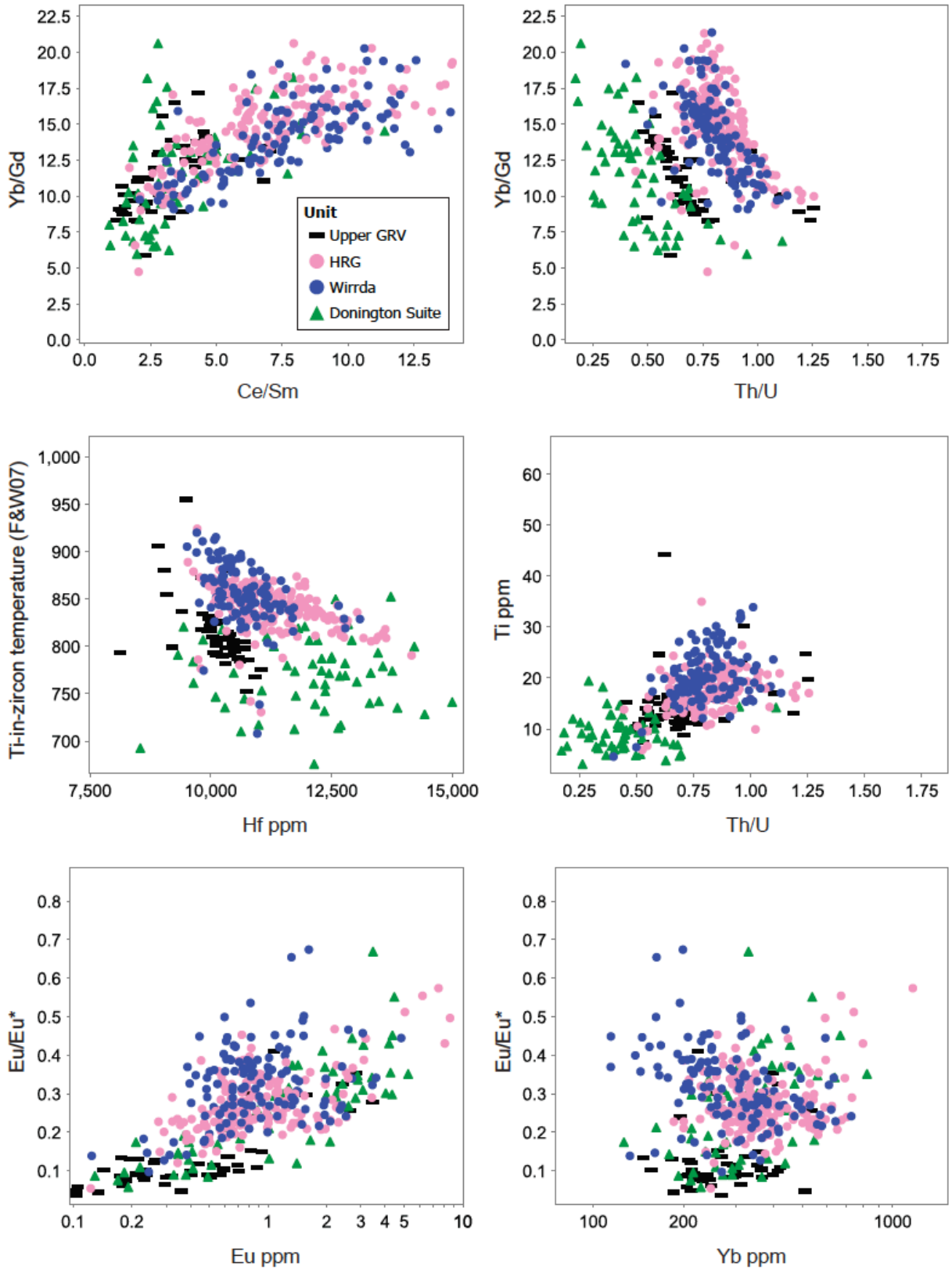
Yb/Gd
Ce/Sm
Unit
Upper GRV
HRG
Wirrda
Donington Suite
Yb/Gd
Th/U
Ti-in-zircon temperature (F&W07)
Hf ppm
Ti ppm
Th/U
Eu/Eu*
Eu ppm
Eu/Eu*
Yb ppm

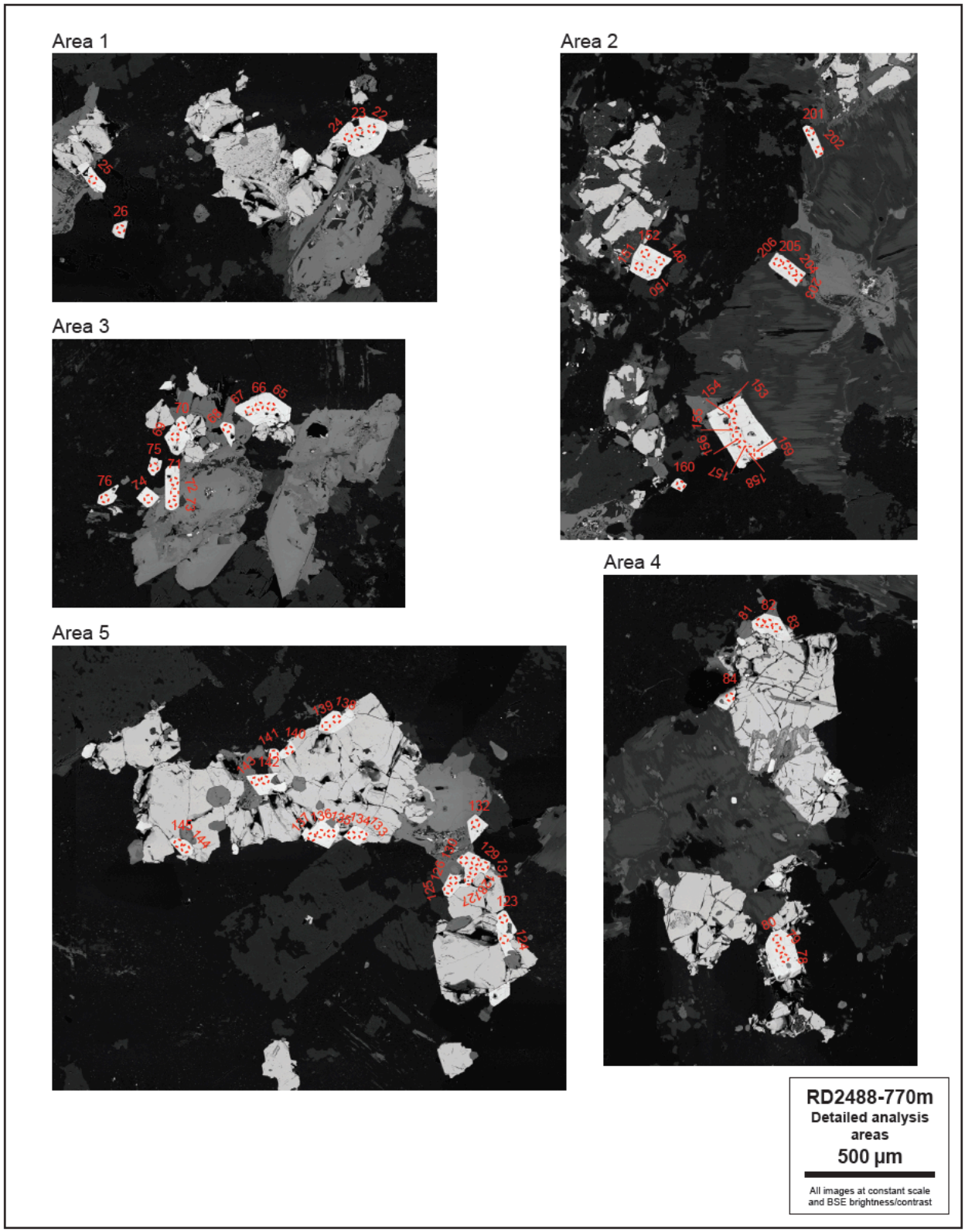
Area 1
Area 2
Area 3
Area 4
Area 5
RD2488-770m
Detailed analysis areas
500 µm
All images at constant scale and BSE brightness/contrast

Area 6

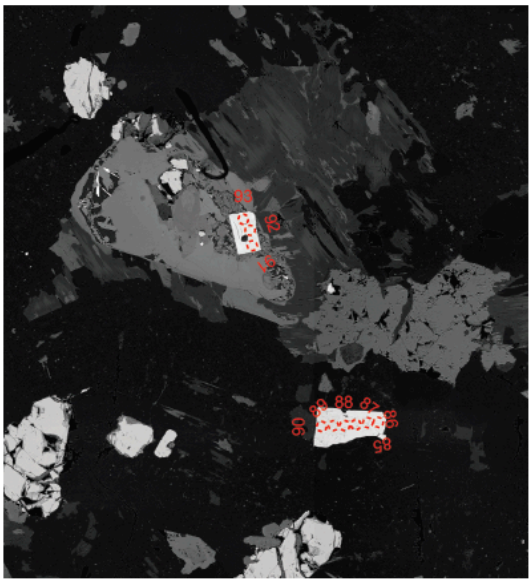

Area 7

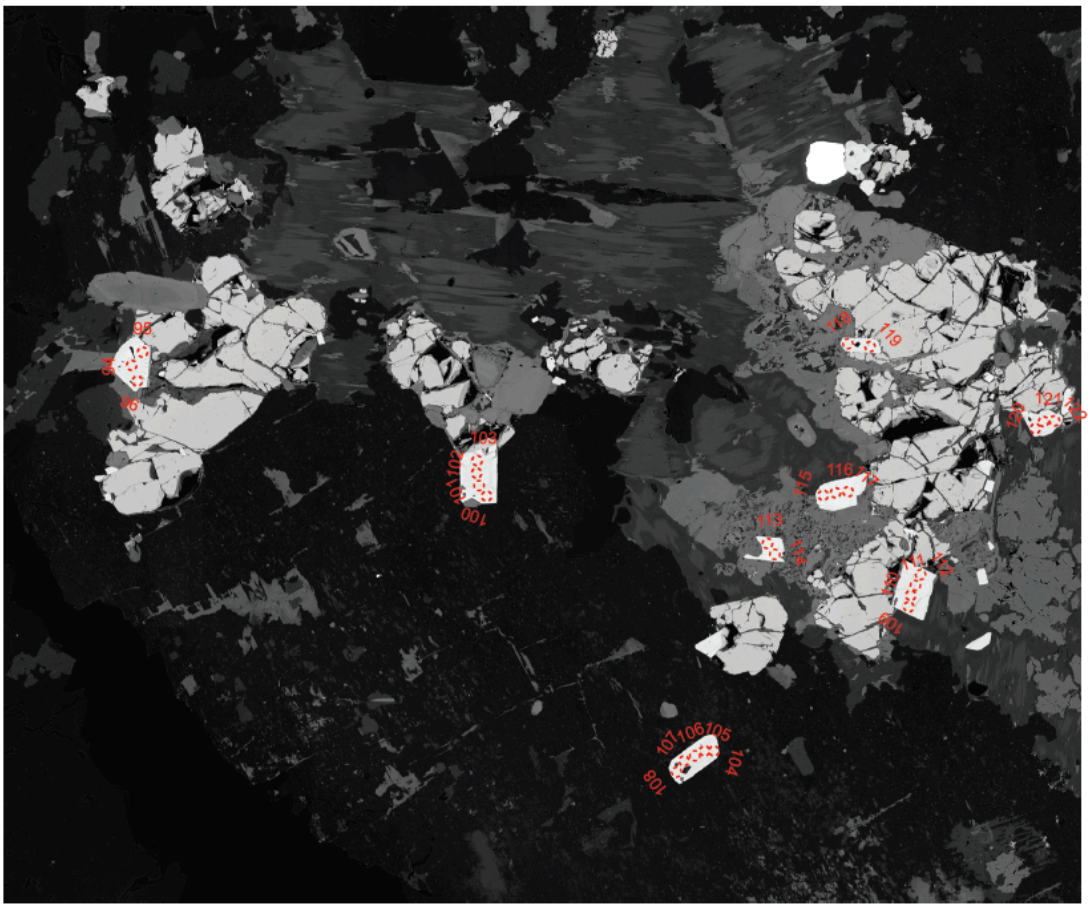

RD2488-770m
Detailed analysis areas
500 µm
All images at constant scale and BSE brightness/contrast

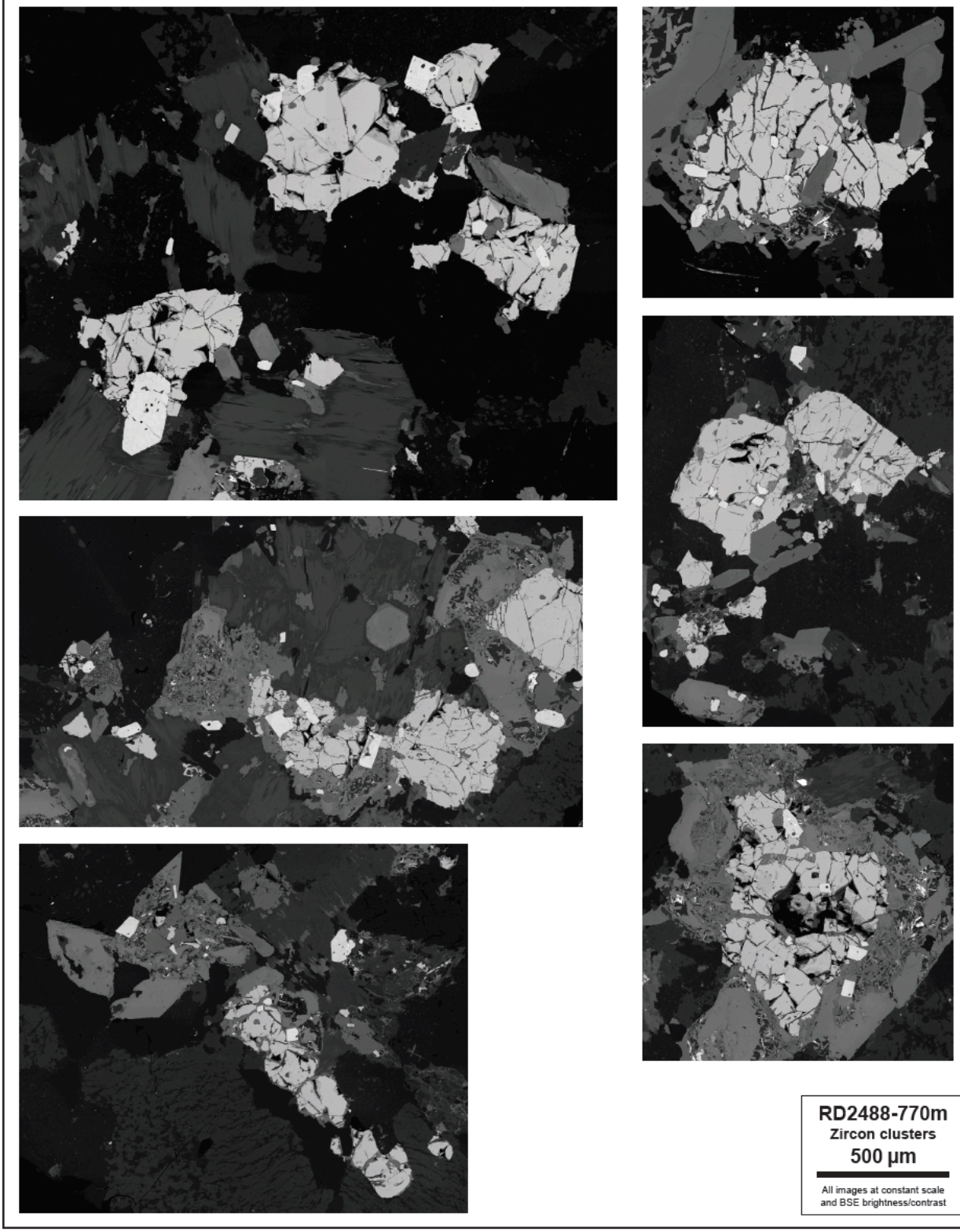
RD2488-770m
Zircon clusters
500 µm
All images at constant scale
and BSE brightness/contrast

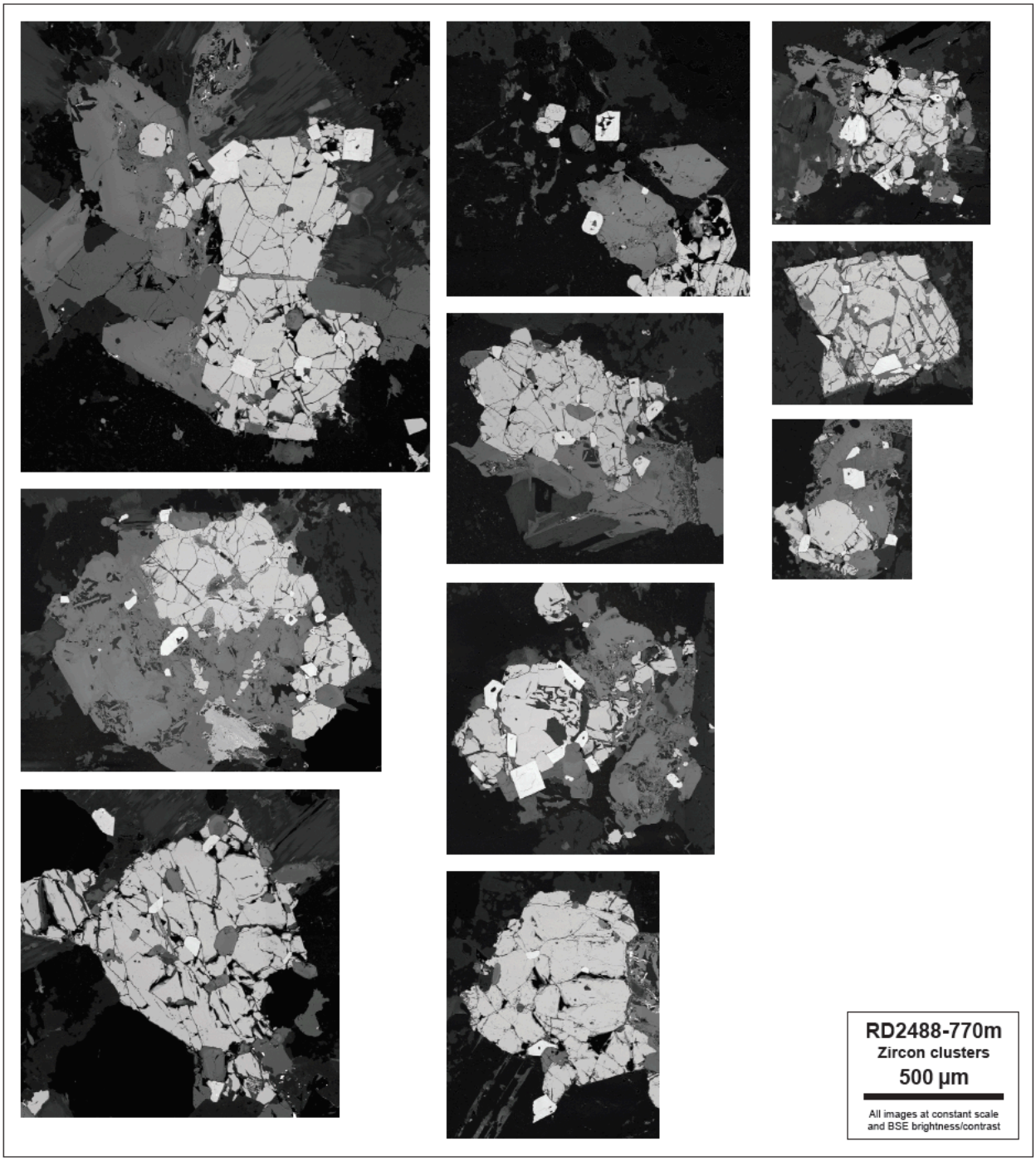
RD2488-770m
Zircon clusters
500 µm
All images at constant scale
and BSE brightness/contrast


RD2488-780m
Zircon CL images
150 µm
All images at constant scale and CL brightness/contrast

Area 1

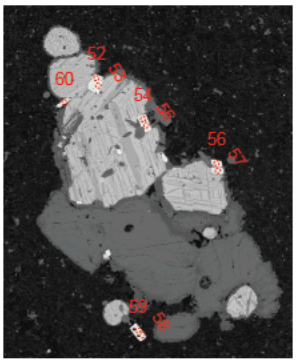

Area 2

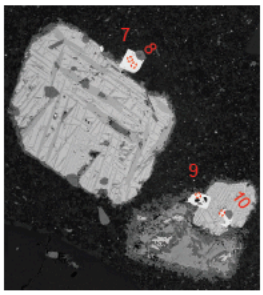

Area 3

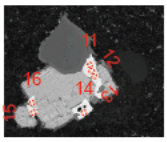

GRVPW20
Detailed analysis areas
600 µm

All images at constant scale and BSE brightness/contrast

Area 4

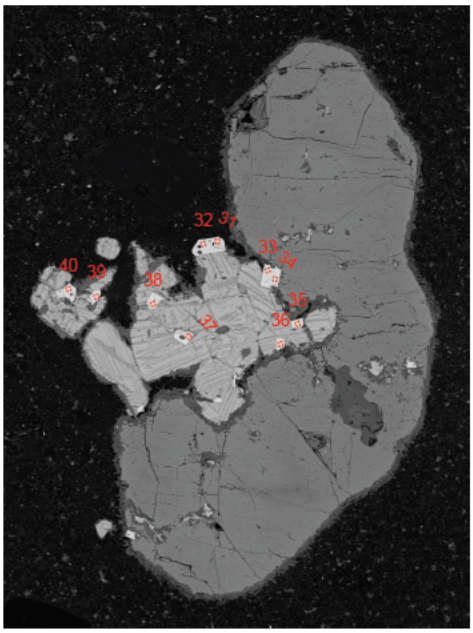

Area 5

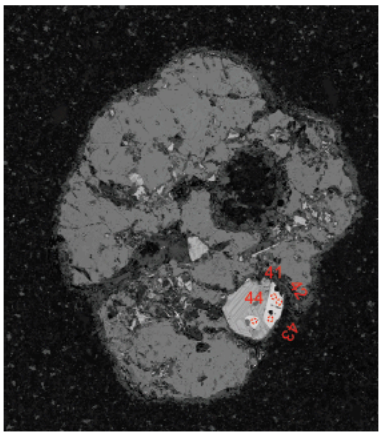

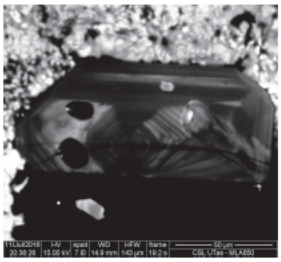

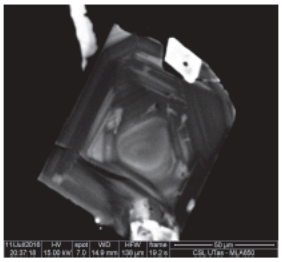

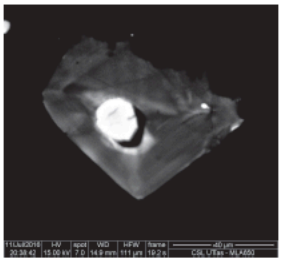

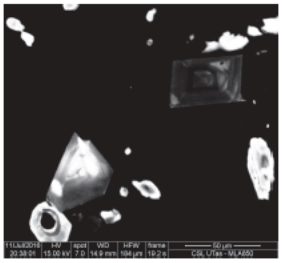

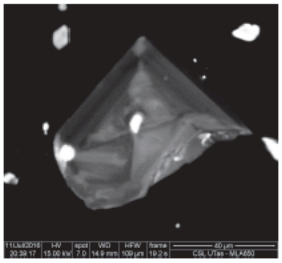

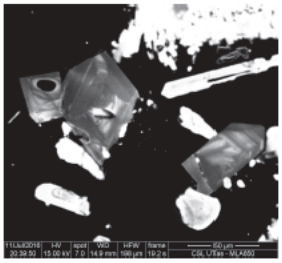

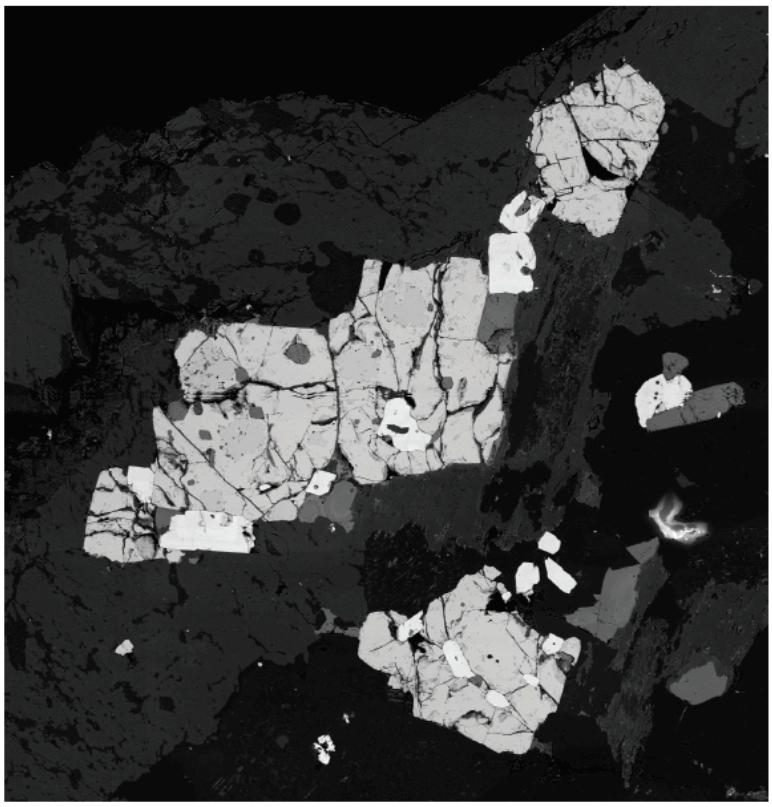

OFD3-450m
Zircon clusters
500 µm

All images at constant scale and BSE brightness/contrast


HRD1-382m
Zircon CL images
150 µm
All images at constant scale and CL brightness/contrast

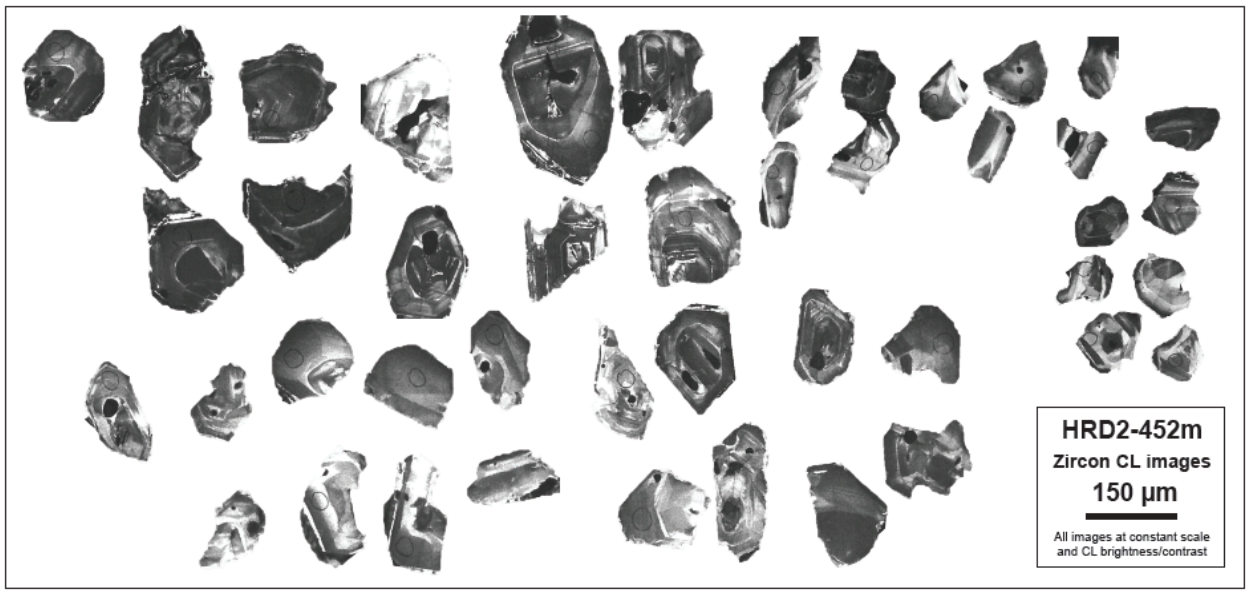
HRD2-452m
Zircon CL images
150 µm
All images at constant scale and CL brightness/contrast

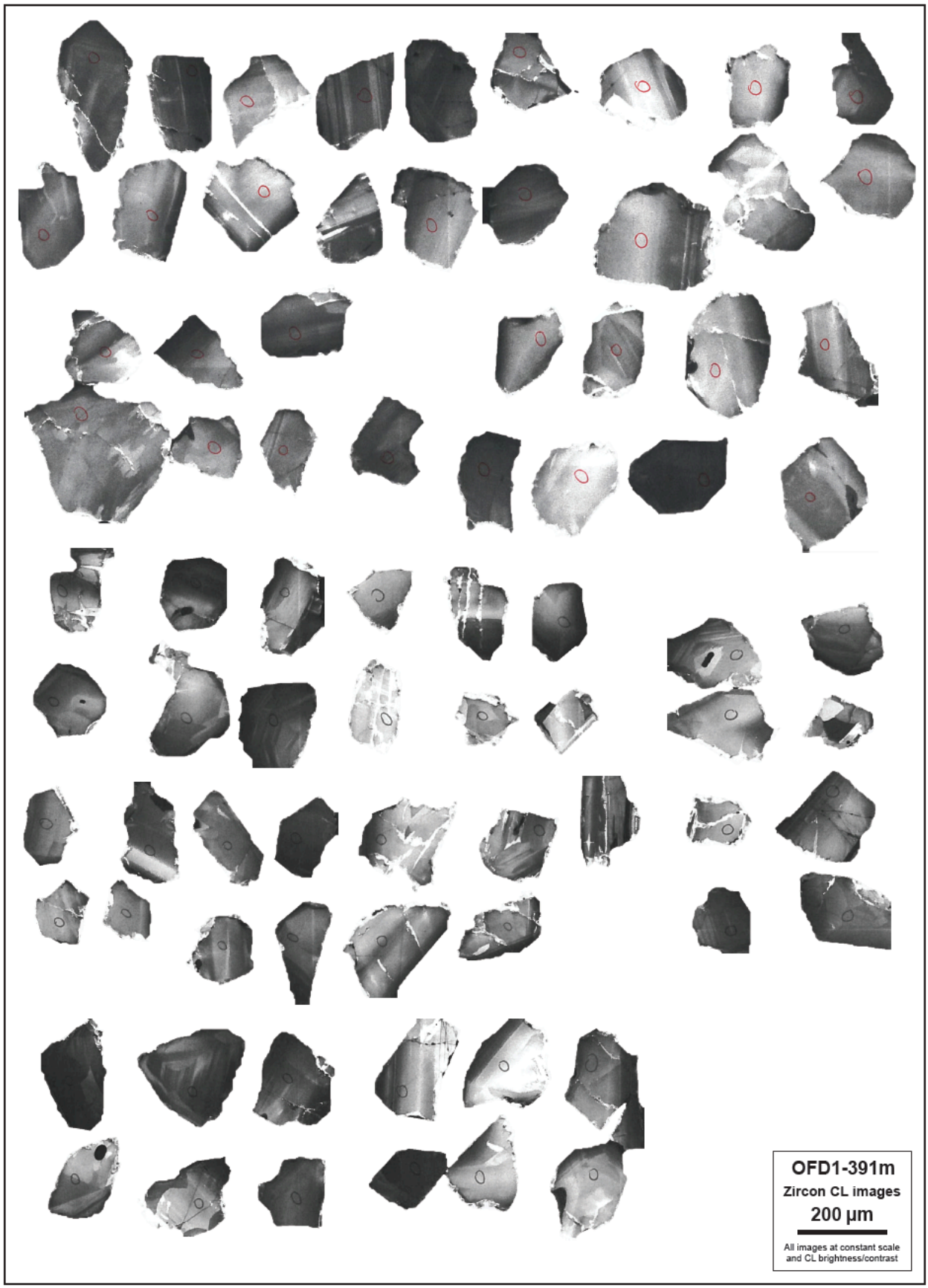
OFD1-391m
Zircon CL images
200 µm
All images at constant scale
and CL brightness/contrast

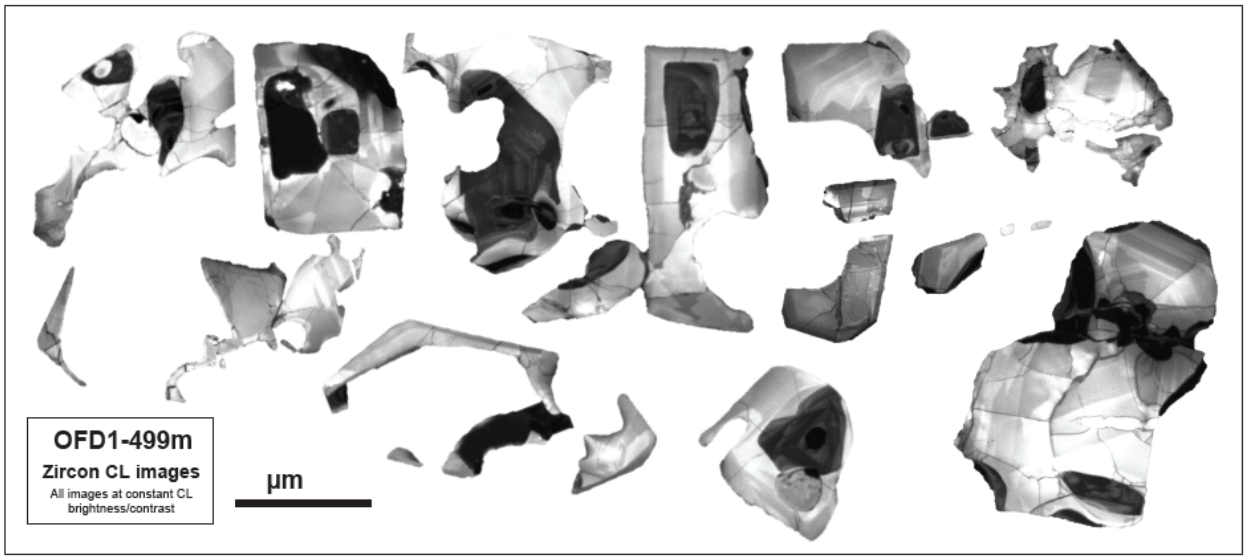
OFD1-499m
Zircon CL images
All images at constant CL brightness/contrast
µm

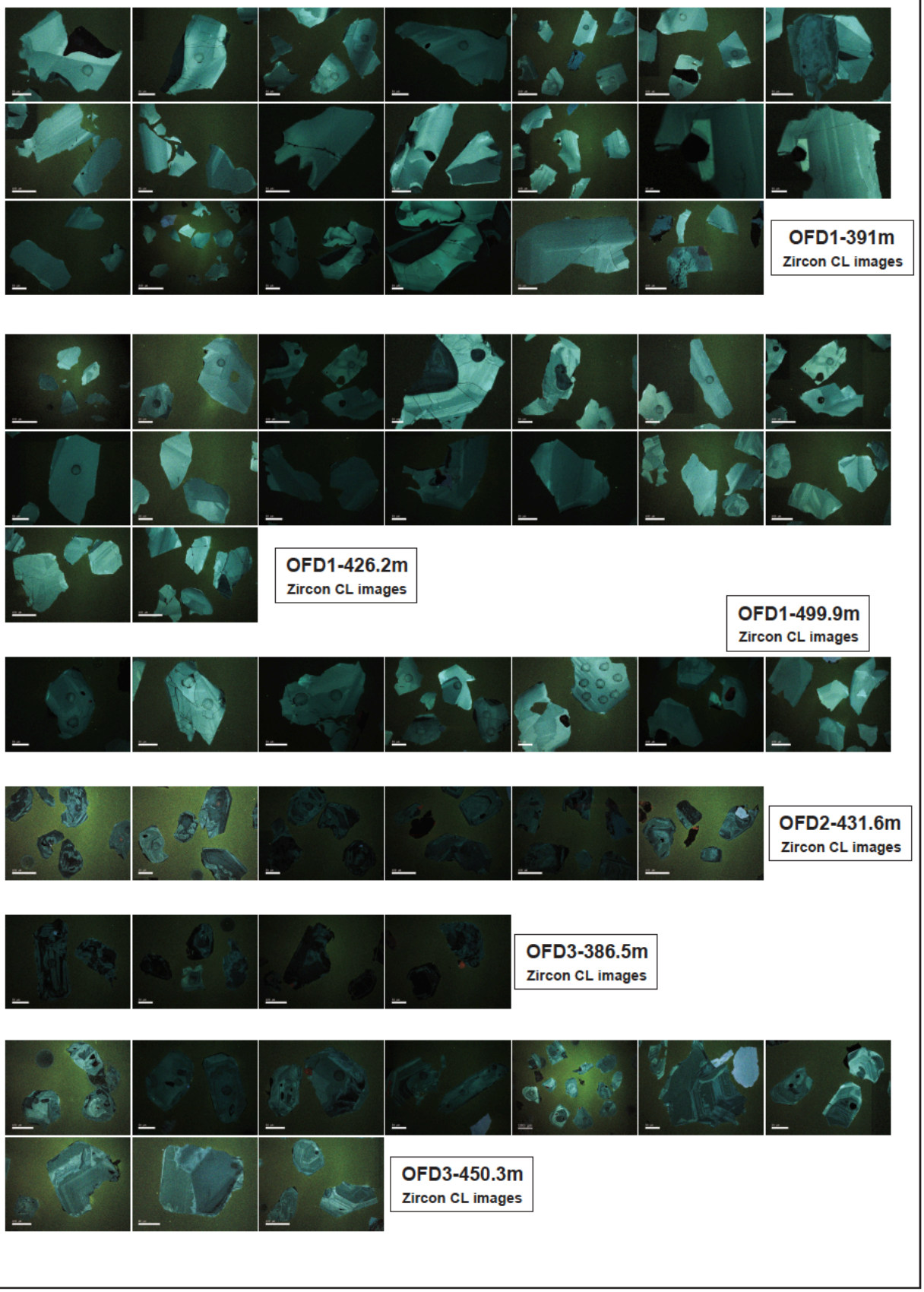
OFD1-391m
Zircon CL images
OFD1-426.2m
Zircon CL images
OFD1-499.9m
Zircon CL images
OFD2-431.6m
Zircon CL images
OFD3-386.5m
Zircon CL images
OFD3-450.3m
Zircon CL images

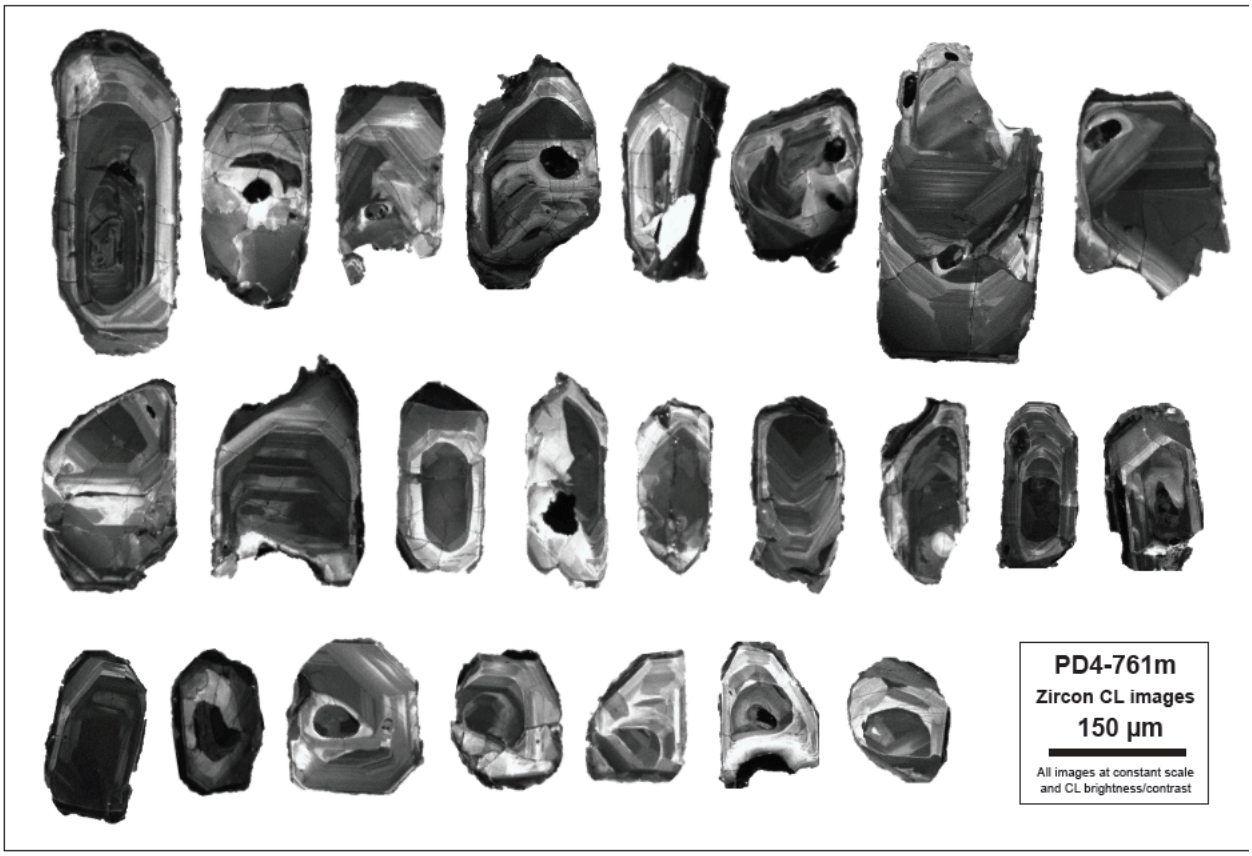
PD4-761m
Zircon CL images
150 µm
All images at constant scale and CL brightness/contrast

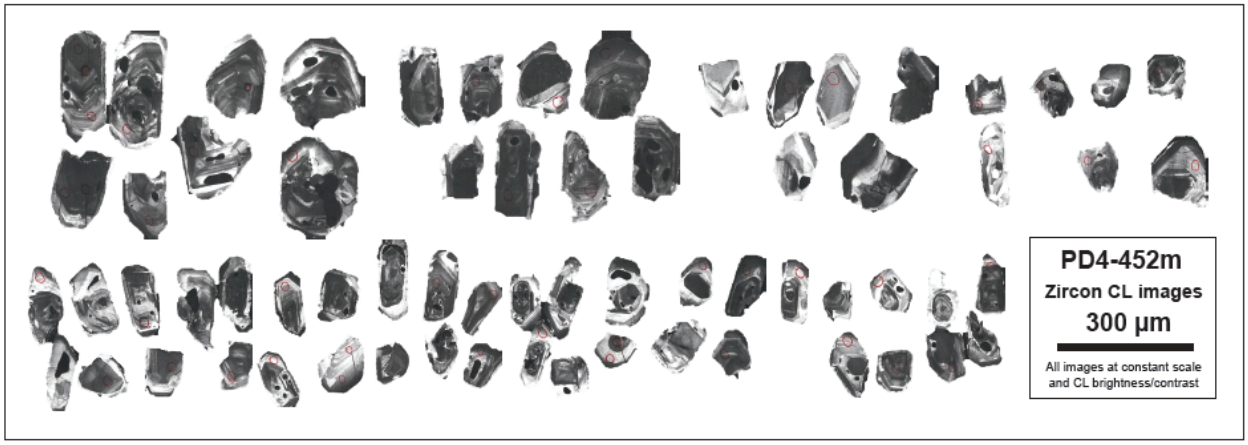
PD4-452m
Zircon CL images
300 µm
All images at constant scale and CL brightness/contrast

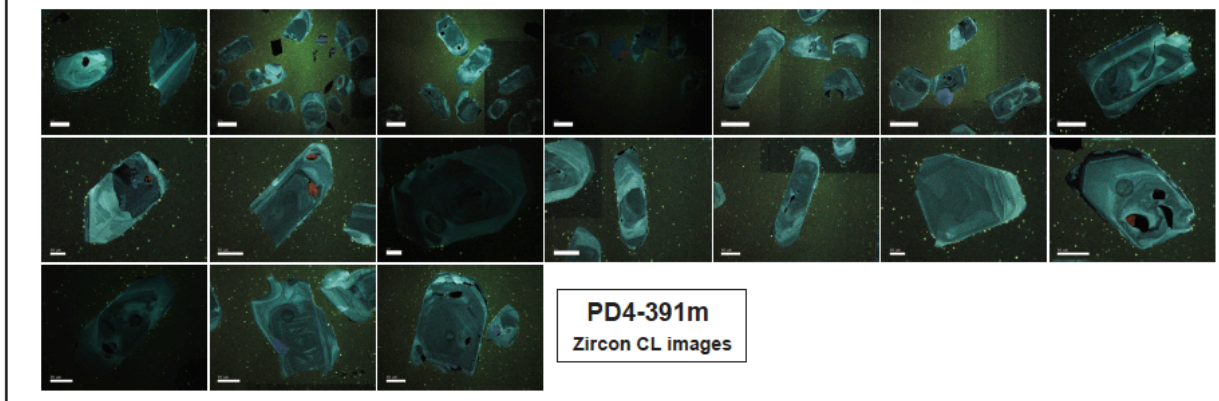

PD4-391m
Zircon CL images

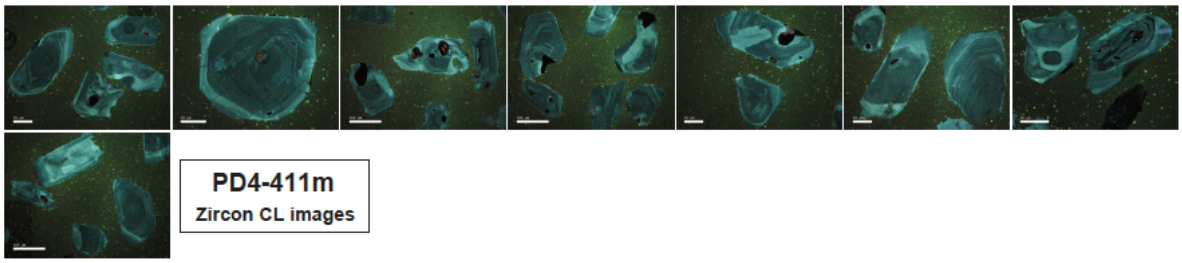

PD4-411m
Zircon CL images

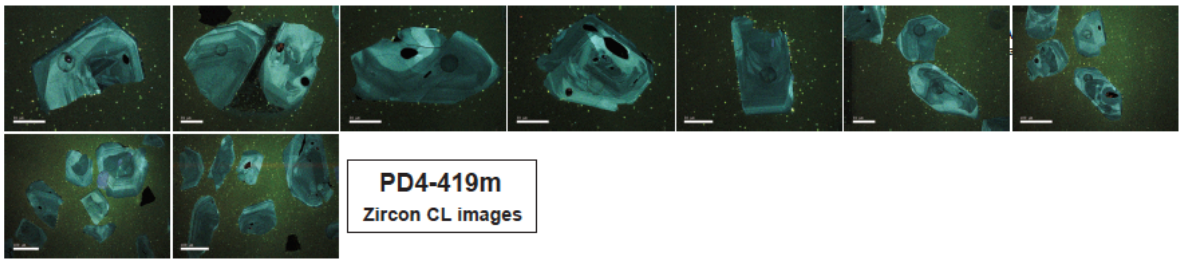

PD4-419m
Zircon CL images

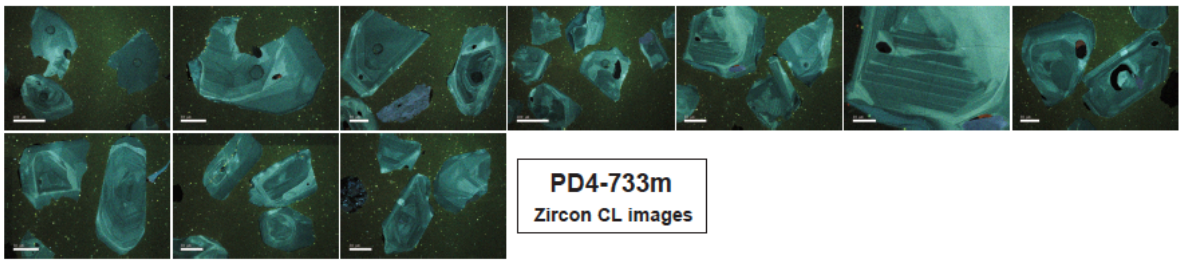

PD4-733m
Zircon CL images

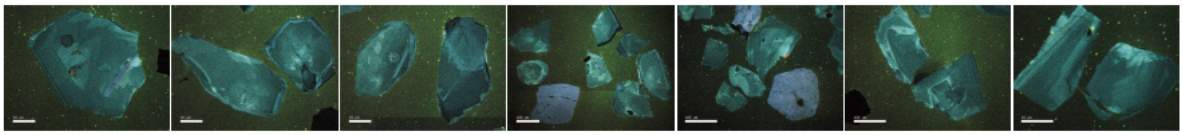

PD4-761
Zircon CL images

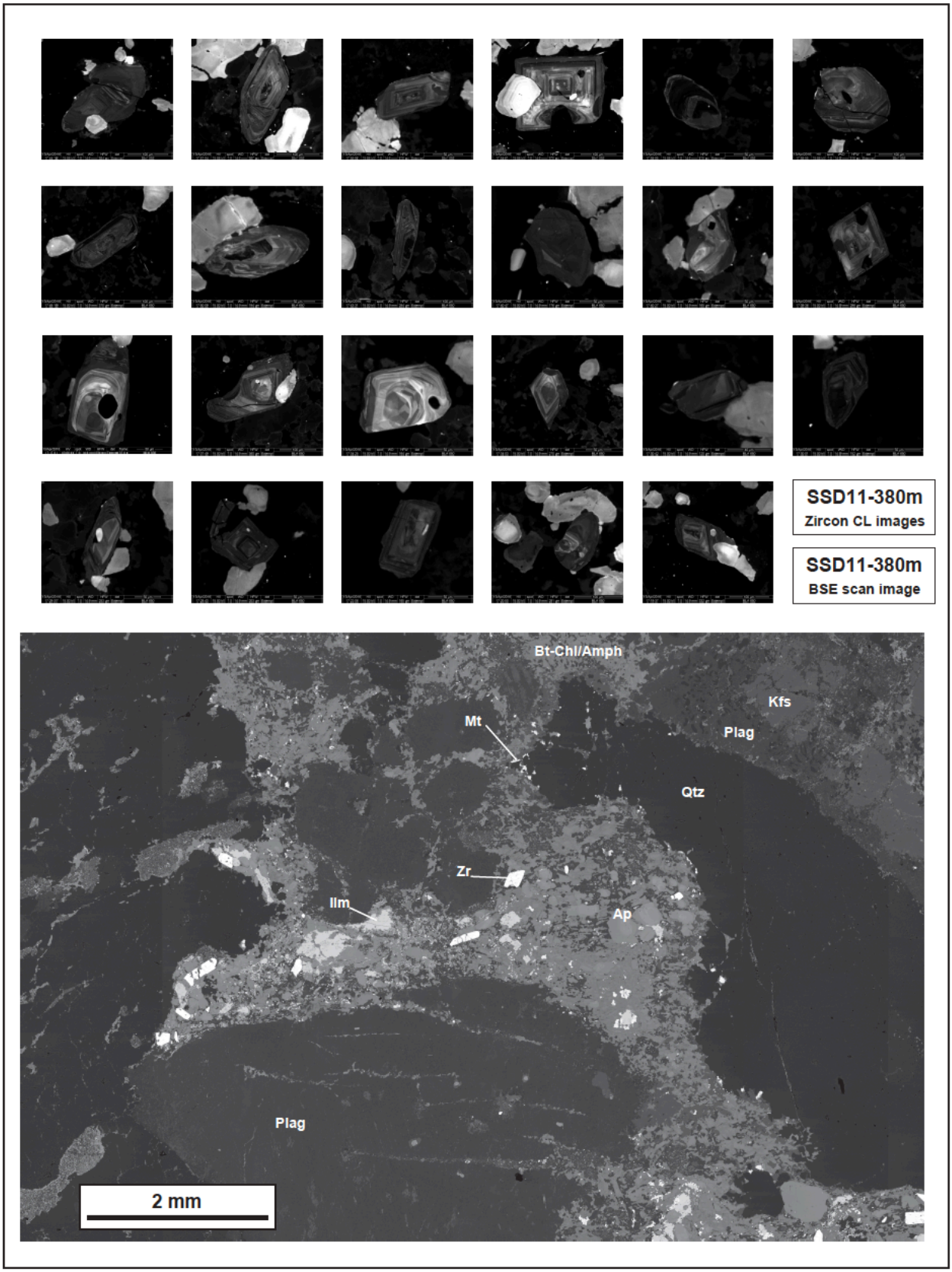
SSD11-380m
Zircon CL images
SSD11-380m
BSE scan image
Bt-Chl/Amph
Kfs
Mt
Plag
Qtz
Zr
Ilm
Ap
Plag
2 mm

Appendix B.1 *In situ* growth of zircon

Minerals that include Y, Ti, Ca and the REE as major structural components can accommodate Zr in significant concentrations (Bea, Montero, & Ortega, 2006). The Fe–Ti oxides and titanite in the Upper GRV and the RDG have the potential to be significant Zr-bearing phases and warrant consideration as a source of Zr for in situ formation of zircon. Titanomagnetite from the Eucarro Rhyolite and Moonaree Dacite contains around 200 ppm Zr and up to 300 ppm in the Pondanna Dacite (Ferguson, Ehrig, & Meffre, 2019). Ilmenite tested from these lavas contains ~900 ppm Zr. The Zr content of magnetite from the RDG is below the limits of detection (< 0.05 ppm Zr), whereas primary titanite contains between 500 and 1600 ppm Zr (see Supplementary Data Table S5B).

The in situ formation of zircon from Zr-bearing minerals can be evaluated using the formulation of Fraser, Ellis, and Eggins (1997). To grow a 100 μm cube of zircon from titanomagnetite containing 200 ppm Zr (Eucarro Rhyolite), or 900 ppm Zr in ilmenite (Yardea Dacite), requires a volume of titanomagnetite or ilmenite, ~3,300 or ~750 times greater than zircon, respectively. This equates to a 1.6 mm cube of titanomagnetite, or a 1 mm cube of ilmenite, per zircon (assuming all Zr is expelled). To have grown eight zircon with lengths greater than 80 μm, similar to those observable in typical zircon-rich clusters (just in the plane of observation), requires an initial concentration of > 1,600 ppm Zr in a 1.6 mm cube of titanomagnetite. If zircon grains are similarly abundant in the remainder of the clusters outside of the plane of observation, a much higher initial concentration of Zr in Fe–Ti oxides is required. While these calculations indicate that the high abundance of zircon in crystal clusters is not primarily due exsolution of Zr from Fe–Ti oxides, it is likely that Zr exsolved during cooling of the RDG contributed to the growth of zircon already present and also formed additional, small zircon crystals around and within Fe–Ti oxides (e.g. Zr-rich patches shown in Figure 3) that could have acted as seed crystals that focussed further uptake of Zr and growth of zircon. Ilmenite in calc alkaline mafic and felsic rocks typically contain only a few tens to hundreds of ppm Zr and magnetite in calc alkaline granitic rocks only have a few ppm Zr (Bea *et al.*, 2006). Xenocrystic Fe–Ti oxides from mantle-derived magmas are the only examples of minerals that contain concentrations of Zr (Tompkins & Haggerty, 1985) sufficient to form the abundant zircon observed in GRV and RDG crystal clusters. Therefore, the observed volume of zircon in the zircon-rich clusters cannot be accounted for by the release of Zr from titanomagnetite and ilmenite in the GRV or RDG. Furthermore, the overwhelming volume of zircon in the Upper GRV and RDG do not show morphological features of zircon formed in situ at subsolidus conditions (e.g. Bingen, Austrheim, & Whitehouse, 2001; Charlier, Skår, Korneliussen, Duchesne, & Vander Auwera, 2007; Morisset & Scoates, 2008). Euhedral zircon from both the Eucarro Rhyolite and the RDG are characterised by short, squat pyramidal terminations ([101]>>[211]), and simple, four- to eight-sided prisms ([100]>>[110]). The simplicity of the prisms indicates a high temperature of formation and the squat pyramids indicates growth under Al < Na + K + Ca conditions (Pupin, 1980), similar to conditions inferred to be prevalent during development of the Upper GRV and RDG (e.g., zircon saturation thermometry, Ti-in-zircon crystallisation temperatures, whole rock geochemistry) (this study; Creaser, 1989; Creaser & White, 1991).

Appendix B.2 Xenocrystic or autocrystic zircon?

Xenocrystic or restitic zircon in igneous rocks have often been identified through their distinctive pre-magmatic U–Pb ages (e.g. Bea, Montero, González-Lodeiro, & Talavera, 2007). Pre-existing (inherited) zircon in partial melts of older intrusive, sedimentary or metamorphic rocks may withstand resorption if the host melt is low-temperature, wet, and Zr-saturated (Chappell, Bryant, Wyborn, White, & Williams, 1998; Kemp, Whitehouse, Hawkesworth, & Alarcon, 2005; Miller, McDowell, & Mapes, 2003; Watson, 1996). Inherited zircon crystals may be compositionally distinct and show different habits and sizes to newly formed zircon (autocrystic or antecrystic) and may show a greater variety of zonation styles and resorption features (e.g. Hoskin & Schaltegger, 2003; Kemp *et al.*, 2005).

A small subset of GRV-RDG zircon have significantly larger grain sizes than the remaining zircon population (Figure 4b), and potentially represent: (1) inherited crystals, (2) crystals with inherited

cores, (3) part of the regular zircon population, or (4) resorption survivors/antecrysts (e.g. Miller, Matzel, Miller, Burgess, & Miller, 2007). These zircon do not have geochemical characteristics that set them apart from the regular zircon population, however, one particularly large zircon has a core which returned amongst the lowest Hf and highest Ti of all analysed zircon, consistent with the predicted composition of an early crystallised zircon (Figures 7 and 8). Truncated zonation observed in a minority of zircon could be related to partial resorption of cognate magmatic zircon, rather than partial resorption of inherited zircon. Moreover, despite the large outliers, there does not appear to be a multi-modal zircon grain size distribution in the GRV and RDG. The grain size distribution for both the Upper GRV and RDG indicates near steady-state zircon crystallisation. None of these features are indicative of significance zircon inheritance in the Upper GRV or RDG.

As U–Pb geochronology does not reveal any concordant zircon populations with ages older than *ca* 1590 Ma, and our ages are within error of previous precise age determinations (Cherry *et al.*, 2018), it is unlikely that there is a significant proportion of inherited zircon in the areas of the Eucarro Rhyolite and RDG sampled, or that the zircon-rich clusters include a significant (or any) inherited component. Previous geochronological studies of the Upper GRV (Creaser & Cooper, 1993; Fanning, Flint, Parker, Ludwig, & Blissett, 1988; Jagodzinski, Reid, Crowley, McAvaney, & Wade, 2016; Jagodzinski, Reid, Crowley, McAveney, & Wade, submitted) and RDG (Cherry *et al.*, 2018; Creaser & Cooper, 1993; Jagodzinski, 2014; Mortimer *et al.*, 1988) have also shown no apparent zircon inheritance.

There is a strong temperature and compositional control on Zr solubility in aluminosilicate melts. Zircon is stable to the highest temperatures in highly evolved subalkaline melts and correspondingly, is most soluble in alkaline mafic melts at high temperatures (Watson & Harrison, 1983). The HS are silica-saturated and straddle the alkaline-subalkaline divide (Creaser, 1989; Stewart & Foden, 2003), while the RDG is an alkali granite (Ferguson *et al.*, 2019; Kontonikas-Charos *et al.*, 2017), suggesting that zircon was soluble in high temperature HS parental melts. Zircon dissolution is rapid if zircon crystals come into contact with a zircon-undersaturated melt (cf. Watson, 1996), and there is no evidence of extreme Zr enrichment in the Upper GRV or RDG which would be required for survival of xenocrystic zircon in the parental melts. Thus the high Zr content of the Upper GRV lavas and RDG are in agreement with theoretical predictions based on Zr solubility in natural melts (e.g. Watson & Harrison, 1983), empirical studies (Miller *et al.*, 2003), and the high temperature nature of Hiltaba magmatism. Any appreciably older zircon that may occur in these rocks would have likely been incorporated from magma reservoir wall rocks, once the magma was below the zircon saturation temperature, to prevent resorption of xenocrystic zircon introduced at this stage.

As in situ growth of zircon was unlikely to have been significant and inherited and xenocrystic zircon do not appear to be present, the majority of zircon in the Upper GRV and RDG are inferred to have crystallised within their parental magmatic systems. The zircon show oscillatory zonation with morphologies indicating growth from a silicate melt (e.g. Hanchar & Miller, 1993) and no widespread evidence for metamorphic recrystallisation (Tables 2 and 3).

References

Bea, F., Montero, P., González-Lodeiro, F., & Talavera, C. (2007). Zircon Inheritance Reveals Exceptionally Fast Crustal Magma Generation Processes in Central Iberia during the Cambro-Ordovician. *Journal of Petrology, 48*(12), 2327–2339. doi:10.1093/petrology/egm061

Bea, F., Montero, P., & Ortega, M. (2006). A LA–ICP–MS evaluation of Zr reservoirs in common crustal rocks: implications for Zr and Hf geochemistry, and zircon-forming processes. *The Canadian Mineralogist, 44*(3), 693–714. doi:10.2113/gscanmin.44.3.693

Bingen, B., Austrheim, H., & Whitehouse, M. (2001). Ilmenite as a source for zirconium during high-grade metamorphism? Textural evidence from the Caledonides of Western Norway and implications for zircon geochronology. *Journal of Petrology, 42*(2), 355–375. doi:10.1093/petrology/42.2.355

Chappell, B. W., Bryant, C. J., Wyborn, D., White, A. J. R., & Williams, I. S. (1998). High- and Low-Temperature I-type Granites. *Resource Geology, 48*(4), 225–235. doi:10.1111/j.1751-3928.1998.tb00020.x

Charlier, B., Skår, Ø., Korneliussen, A., Duchesne, J.-C., & Vander Auwera, J. (2007). Ilmenite composition in the Tellnes Fe–Ti deposit, SW Norway: fractional crystallization, postcumulus evolution and ilmenite–zircon relation. *Contributions to Mineralogy and Petrology, 154*(2), 119–134. doi:10.1007/s00410-007-0186-8

Cherry, A. R., Ehrig, K., Kamenetsky, V. S., McPhie, J., Crowley, J. L., & Kamenetsky, M. B. (2018). Precise geochronological constraints on the origin, setting and incorporation of ca. 1.59 Ga surficial facies into the Olympic Dam Breccia Complex, South Australia. *Precambrian Research, 315*, 162–178. https://doi.org/10.1016/j.precamres.2018.07.012

Creaser, R. A. (1989). The geology and petrology of Middle Proterozoic felsic magmatism of the Stuart Shelf, South Australia. (PhD), La Trobe University.

Creaser, R. A., & Cooper, J. A. (1993). U–Pb geochronology of middle Proterozoic felsic magmatism surrounding the Olympic Dam Cu–U–Au–Ag and Moonta Cu–Au–Ag deposits, South Australia. *Economic Geology, 88*(1), 186–197.

Creaser, R. A., & White, A. J. (1991). Yardea Dacite—large-volume, high-temperature felsic volcanism from the Middle Proterozoic of South Australia. *Geology, 19*(1), 48–51. doi:10.1130/0091-7613(1991)019<0048:YDLVHT>2.3.CO;2

Fanning, C. M., Flint, R. B., Parker, A. J., Ludwig, K. R., & Blissett, A. H. (1988). Refined Proterozoic evolution of the Gawler Craton, South Australia, through U–Pb zircon geochronology. *Precambrian Research, 40–41*, 363–386. https://doi.org/10.1016/0301-9268(88)90076-9

Ferguson, M. R. M., Ehrig, K., & Meffre, S. (2019). Insights into magma histories through silicate–oxide crystal clusters: Linking the Hiltaba Suite intrusive rocks to the Gawler Range Volcanics, Gawler Craton, South Australia. *Precambrian Research, 321*, 103–122. https://doi.org/10.1016/j.precamres.2018.11.015

Fraser, G., Ellis, D., & Eggins, S. (1997). Zirconium abundance in granulite-facies minerals, with implications for zircon geochronology in high-grade rocks. *Geology, 25*(7), 607–610. doi:10.1130/0091-7613(1997)025<0607:ZAIGFM>2.3.CO;2

Hanchar, J. M., & Miller, C. F. (1993). Zircon zonation patterns as revealed by cathodoluminescence and backscattered electron images: Implications for interpretation of complex crustal histories. *Chemical Geology, 110*(1–3), 1–13. https://doi.org/10.1016/0009-2541(93)90244-D

Hoskin, P. W. O., & Schaltegger, U. (2003). The Composition of Zircon and Igneous and Metamorphic Petrogenesis. *Reviews in Mineralogy and Geochemistry, 53*(1), 27–62. doi:10.2113/0530027

Jagodzinski, E. A. (2014). *The age of magmatic and hydrothermal zircon at Olympic Dam*. Paper presented at the 2014 Australian Earth Sciences Convention, Newcastle, Australia.

Jagodzinski, E. A., Reid, A., Crowley, J., McAvaney, S. O., & Wade, C. (2016). *New Ca-TIMS dates for the Gawler Range Volcanics: stratigraphic issues arising from results, and future directions*. Paper presented at the Geological Survey of South Australia Discovery Day 2016, Adelaide. http://minerals.statedevelopment.sa.gov.au/knowledge_centre/mesa_journal/events/geological_survey_of_south_australia_discovery_day_2016/gssa_dd_presentations/GSSA_DD_Liz_Jagodzinski_1_Dec_2016.pdf

Jagodzinski, E. A., Reid, A. J., Crowley, J. L., McAveney, S., & Wade, C. E. (submitted). Precise zircon U–Pb dating of a Mesoproterozoic silicic large igneous province: the Gawler Range Volcanics and Benagerie Volcanic Suite, South Australia. *Journal of the Geological Society*.

Kemp, A. I. S., Whitehouse, M. J., Hawkesworth, C. J., & Alarcon, M. K. (2005). A zircon U–Pb study of metaluminous (I-type) granites of the Lachlan Fold Belt, southeastern Australia: implications for the high/low temperature classification and magma differentiation processes. *Contributions to Mineralogy and Petrology, 150*(2), 230–249. doi:10.1007/s00410-005-0019-6

Kontonikas-Charos, A., Ciobanu, C. L., Cook, N. J., Ehrig, K., Krneta, S., & Kamenetsky, V. S. (2017). Feldspar evolution in the Roxby Downs Granite, host to Fe-oxide Cu–Au–(U) mineralisation at Olympic Dam, South Australia. *Ore Geology Reviews, 80*, 838–859.

Miller, C. F., McDowell, S. M., & Mapes, R. W. (2003). Hot and cold granites? Implications of zircon saturation temperatures and preservation of inheritance. *Geology, 31*(6), 529–532. doi:10.1130/0091-7613(2003)031<0529:hacgio>2.0.co;2

Miller, J. S., Matzel, J. E. P., Miller, C. F., Burgess, S. D., & Miller, R. B. (2007). Zircon growth and recycling during the assembly of large, composite arc plutons. *Journal of Volcanology and Geothermal Research, 167*(1–4), 282–299. doi:10.1016/j.jvolgeores.2007.04.019

Morisset, C.-E., & Scoates, J. S. (2008). Origin of zircon rims around ilmenite in mafic plutonic rocks of Proterozoic anorthosite suites. *The Canadian Mineralogist, 46*(2), 289–304. doi:10.3749/canmin.46.2.289

Mortimer, G. E., Cooper, J. A., Paterson, H. L., Cross, K., Hudson, G. R. T., & Uppill, R. K. (1988). Zircon U–Pb dating in the vicinity of the Olympic Dam Cu–U–Au deposit, Roxby Downs, South Australia. *Economic Geology, 83*(4), 694–709. doi:10.2113/gsecongeo.83.4.694

Pupin, J. P. (1980). Zircon and granite petrology. *Contributions to Mineralogy and Petrology, 73*(3), 207–220. doi:10.1007/bf00381441

Stewart, K., & Foden, J. D. (2003). *Mesoproterozoic granites of South Australia, Report Book 2003/00015*. Adelaide: Department of Primary Industries and Resources, South Australia.

Tompkins, L. A., & Haggerty, S. E. (1985). Groundmass oxide minerals in the Koidu kimberlite dikes, Sierra Leone, West Africa. *Contributions to Mineralogy and Petrology, 91*(3), 245–263. doi:10.1007/bf00413351

Watson, E. B. (1996). Dissolution, growth and survival of zircons during crustal fusion: kinetic principles, geological models and implications for isotopic inheritance. *Geological Society of America Special Papers, 315*, 43–56. doi:10.1130/0-8137-2315-9.43

Watson, E. B., & Harrison, T. M. (1983). Zircon saturation revisited: temperature and composition effects in a variety of crustal magma types. *Earth and Planetary Science Letters, 64*(2), 295–304. http://dx.doi.org/10.1016/0012-821X(83)90211-X